AGU PUBLICATIONS

Water Resources Research

RESEARCH ARTICLE
10.1002/2015WR018389

Special Section:
Modeling highly heterogeneous aquifers: Lessons learned in the last 30 years from the MADE experiments and others

Correspondence to:
Harald Klammler,
haki@ufl.edu

Citation:
Klammler, H., K. Hatfield, M. A. Newman, J. Cho, M. D. Annable, B. L. Parker, J. A. Cherry, and I. Perminova (2016), A new device for characterizing fracture networks and measuring groundwater and contaminant fluxes in fractured rock aquifers, *Water Resour. Res.*, *52*, 5400–5420, doi:10.1002/2015WR018389.

Received 17 NOV 2015
Accepted 19 JUN 2016
Accepted article online 22 JUN 2016
Published online 16 JUL 2016

A new device for characterizing fracture networks and measuring groundwater and contaminant fluxes in fractured rock aquifers

Harald Klammler[1], Kirk Hatfield[1], Mark A. Newman[1], Jaehyun Cho[1], Michael D. Annable[1], Beth L. Parker[2], John A. Cherry[2], and Irina Perminova[3]

[1]Engineering School of Sustainable Infrastructure and Environment (ESSIE), University of Florida, Gainesville, Florida, USA, [2]Centre for Applied Groundwater Research, University of Guelph, School of Engineering, Guelph Ontario, Canada, [3]Department of Chemistry, Lomonosov Moscow State University, Moscow 119991, Russia

Abstract This paper presents the fundamental theory and laboratory test results on a new device that is deployed in boreholes in fractured rock aquifers to characterize vertical distributions of water and contaminant fluxes, aquifer hydraulic properties, and fracture network properties (e.g., active fracture density and orientation). The device, a fractured rock passive flux meter (FRPFM), consists of an inflatable core assembled with upper and lower packers that isolate the zone of interest from vertical gradients within the borehole. The outer layer of the core consists of an elastic fabric mesh equilibrated with a visible dye which is used to provide visual indications of active fractures and measures of fracture location, orientation, groundwater flux, and the direction of that flux. Beneath the outer layer is a permeable sorbent that is preloaded with known amounts of water soluble tracers which are eluted at rates proportional to groundwater flow. This sorbent also captures target contaminants present in intercepted groundwater. The mass of contaminant sorbed is used to quantify cumulative contaminant flux; whereas, the mass fractions of resident tracers lost are used to provide measures of water flux. In this paper, the FRPFM is bench tested over a range of fracture velocities (2–20 m/day) using a single fracture flow apparatus (fracture aperture = 0.5 mm). Test results show a discoloration in visible dye corresponding to the location of the active fracture. The geometry of the discoloration can be used to discern fracture orientation as well as direction and magnitude of flow in the fracture. Average contaminant fluxes were measured within 16% and water fluxes within 25% of known imposed fluxes.

1. Introduction

Estimating contaminant migration and flux in fractured media is quite challenging and perhaps much more difficult than in granular media. One challenge is the variation in groundwater and contaminant fluxes within and between fractures intersecting boreholes resulting from the fact that some fractures are large and perhaps important hydraulically, while others are small but significant in the context of controlling plume structure [*Berkowitz*, 2002; *Neuman*, 2005; *Novakowski et al*., 2006]. Some fractures can possess high contaminant concentrations, but produce low mass fluxes because flow is negligible; whereas, in other locations concentrations can be low but produce high contaminant fluxes because flow is significant [*ITRC*, 2010]. Thus, identifying fractures that produce significant contaminant fluxes is a challenge that cannot be overcome in the absence of measuring these fluxes directly or measuring both constituent concentration and flow within a fracture. Finally, with respect to the challenge of estimating water and contaminant discharges, it is critical to recognize the importance of fracture density and flux variability [*Acar et al*., 2013]. Fractures, that individually produce low contaminant fluxes, can generate large contaminant discharges at the transect scale if fracture density is significant [*Parker et al*., 2012].

At present, cumulative or time-averaged contaminant fluxes are calculated using observed contaminant concentrations from boreholes or screened wells installed in fractured media in combination with depth-average groundwater flows. These flows can be calculated using measured hydraulic transmissivities [*Shapiro et al*., 2007] and gradients. Alternatively, they can be directly measured using the borehole (or point) dilution method in open boreholes or in limited intervals thereof using straddle-packers [*Garcia Gutierrez*

et al., 1997; *Xu et al*., 1997; *Novakowski et al*., 2006]. This approach typically requires extensive aquifer characterization and costly flow and water quality monitoring. Hydrophysical logging [*Tsang et al*., 1990; *Pedler et al*., 1992], heat pulse flow meters [*Kerfoot*, 1992], acoustic Doppler velocimeters [*SonTek*, 1996], and colloidal borescopes [*Department of Energy*, 1993] are tools typically used to reveal much about flows in fractures from deployment in open boreholes [*Wilson et al*., 2001]. Unfortunately, open borehole techniques are not likely to produce accurate estimates of ambient contaminant discharge for at least two reasons [*Shapiro*, 2002; *Sterling et al*., 2005; *Novakowsky et al*., 2006]. First, open boreholes induce magnitude and directional changes in water and contaminant fluxes within and between fractures that do not exist naturally as in the absence of a borehole. Such flow distortions are likely to invalidate an interpretation of concentrations and depth-average discharges as being representative for natural aquifer conditions. Second, water and contaminant fluxes may vary significantly between fractures and over time; therefore, typical short-term or instantaneous measurements of flow and concentration do not generate representative long-term projections of flow, concentration and contaminant discharge.

Lined borehole conditions (i.e., where the borehole wall is sealed against water entering the borehole) are preferred for making water and contaminant flux measurements, because the artificial exchange of water and contaminant between fractures that occurs in open boreholes is minimized. With the exception of the disturbance by the impermeable borehole liner, this establishes significantly "closer to natural" flow conditions in the aquifer. In practice, this lining may be achieved by deploying FLUTe^{TM} or packers along borehole sections [*Cherry et al*., 2007]. FLUTe^{TM} systems have been used with high resolution temperature logging techniques to locate and rank active (flowing) fractures under lined borehole conditions [*Pehme et al*., 2010, 2013, 2014; *Coleman et al*., 2015].

To the best of our knowledge, flows or fluxes in individual fractures have not been measured under lined borehole conditions. The objective of this study was to develop a new technology that directly measures the magnitudes and directions of cumulative water and contaminant fluxes in fractured rock aquifers under lined borehole conditions. The existing passive flux meter [PFM; *Hatfield et al*., 2004; *Annable et al*., 2005] is best suited for screened wells and may allow for significant vertical flow inside the well due to the relatively large hydraulic conductivity of the granular sorbent material. This, and the fact that well screens are commonly equipped with highly conductive filter packs, create unfavorable conditions similar to that of an open borehole discussed above. Thus, a new passive flux meter design is needed that functions under lined borehole conditions in unscreened fractured rock wells, and which is easily installed to large enough depths. Here, we present the concept and laboratory testing results of an innovative fractured rock passive flux meter (FRPFM) that directly measures (1) the locations of hydraulically active fractures, i.e., of fractures conveying groundwater flow; (2) active fracture orientations; (3) directions of groundwater flow in each fracture plane; (4) cumulative magnitudes of groundwater fluxes in fractures; and (5) cumulative magnitudes of contaminant fluxes in fractures.

2. Description of Fractured Rock Passive Flux Meter (FRPFM)

Figure 1 shows a laboratory scale FRPFM prototype with an inflatable core combined with upper and lower end packers. The core is simply a packer (or flexible inflatable liner) covered with an internal nonreactive layer of permeable mesh, which is wrapped in a permeable layer of material derived from activated carbon, ion exchange resin, or similar sorbent material. All of this is encased in a thin external permeable layer of cloth material impregnated with a visible dye. The core inflates separately from the two end packers to provide a mechanism for lining the borehole over the testing section by sealing the core against the face of the borehole. The end packers isolate the zone of interest from vertical gradients between the test section and the neighboring open borehole intervals. Figure 2, depicts the plan view or horizontal cross-sectional view of a FRPFM core in a borehole. Shown is the impermeable internal packer (or inflatable flexible liner), the permeable nonreactive mesh and the two permeable reactive fabric layers of sorbent and external cloth. Once the device is inserted into a well, the FRPFM packer or liner is inflated to bring the permeable external cloth layer in intimate contact with the borehole wall and any fractures intersected by the borehole. The external cloth layer, the underlying permeable sorptive layer, and the permeable mesh work in tandem to passively intercept flow in fractures. Because the inflatable liner or packer is impermeable, groundwater flow does not enter the borehole, but is instead diverted around the borehole though the

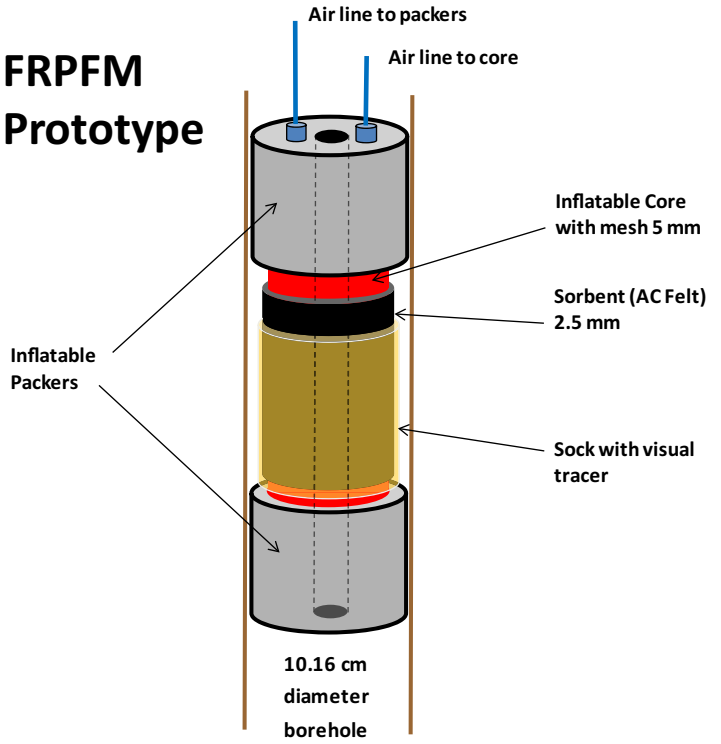

Figure 1. FRPFM Prototype designed with an inflatable core and separate upper and lower end packers. The core is composed of an inner impermeable inflatable packer or flexible liner, surrounded by a permeable layer of nonreactive mesh layer, an internal permeable reactive sorbent layer, and an external visual indication layer.

compound layer. Since both fracture and permeable layer are very thin with respect to borehole diameter, on the up-gradient side of the device the intercepted flow penetrates the sorbent layer vertically above and below the fracture intersection, thus displacing dye and tracers by advective transport (leaving "empty" spots). After flowing circumferentially around the device, intercepted flow again converges to the fracture intersection on the down-gradient side, where it leaves the permeable FRPFM layer. In our conceptual FRPFM model for flux estimation, we do not consider diffusive transport of dye, tracers, or contaminants between the permeable layer and the groundwater in the fracture that is not intercepted by the device. Diffusive transport within the sorbent layer does not affect FRPFM measurements, as it does not impact the amounts of lost dye or tracers nor of sorbed contaminants on the device.

Exposing the FRPFM to flowing groundwater for a selected duration gradually leaches soluble tracers from the sorbent layer and visible dye from the external cloth producing residual distributions of tracers and dye. Visual inspection of the external layer leads to estimates of the following for active fractures: (1) locations along the borehole; (2) number of fractures; (3) individual fracture orientations; (4) groundwater flow direction in fractures; and (5) estimates of the groundwater flux in these fractures. Further analytical analysis of

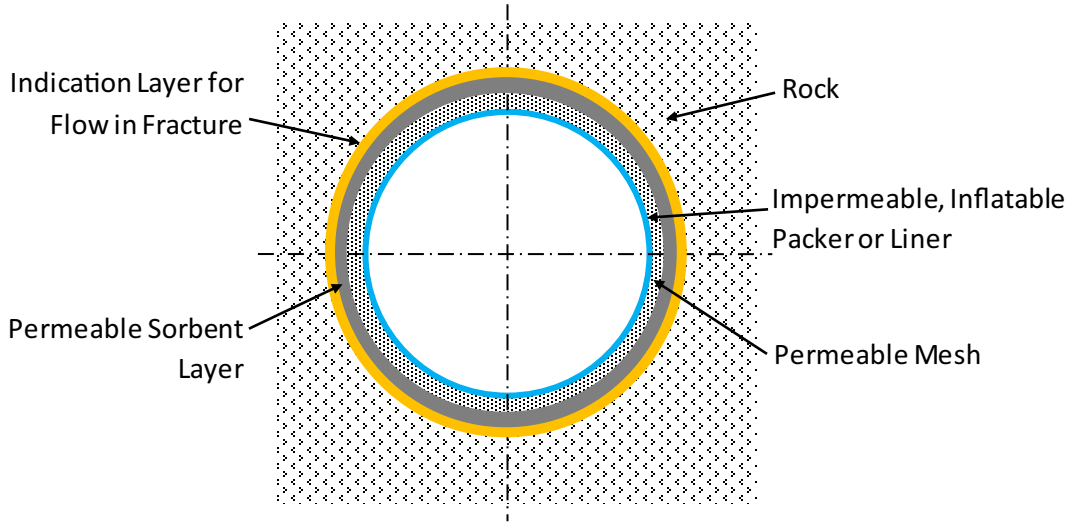

Figure 2. Horizontal cross-section of an FRPFM in an unscreened borehole. The FRPFM core is composed of an inner impermeable inflatable packer or flexible liner, surrounded by permeable layers of nonreactive mesh, a reactive sorbent, and an external fabric for visual indication of flow in a fracture.

soluble residual tracer mass and captured contaminant on the sorbent at indicated locations of active fractures yields: (6) an alternative estimate of cumulative magnitude of groundwater flux; and (7) cumulative magnitude of contaminant flux. Existing borehole imaging technologies can provide measures of fracture characteristics (1) through (3) for fracture apertures greater than 1 mm; however, such technologies do not indicate which fractures convey flow nor do they provide direct measures of flow magnitudes or directions. Thus, the innovations provided by the FRPFM include the ability to locate and characterize active fractures and acquire in situ measurements of direction and magnitude of water and contaminant fluxes in those fractures.

Water and contaminant fluxes are obtained as cumulative magnitudes not only over time but also over fracture aperture and possess the dimensions of water or mass discharge per unit fracture extension in the transverse direction to flow (e.g., cm^3/cm for water flux and mg/cm for contaminant flux). Thus, estimation of a total fracture (or transect) discharge does not depend on highly uncertain measurements of fracture aperture [*Acar et al.*, 2013]. The FRPFM does not provide direct indication of fracture aperture as required for estimating flow velocities; complementary information from other methods may be used for this purpose. However, since the dye or tracer loss indicate the volume of groundwater intercepted, which corresponds exactly to the mass of a contaminant sorbed, contaminant concentrations in the fracture water can be directly estimated from dividing contaminant fluxes by water fluxes. This avoids complications related to mixing between fracture and borehole water, which arise when taking water samples from open borehole intervals [*Shapiro*, 2002]. The mixing effect is exacerbated in large diameter boreholes intersecting fractures with low groundwater fluxes, in which cases the FRPFM may represent and efficient alternative to common grab or low flow sampling for measuring contaminant concentrations.

3. Flow and Transport Through a FRPFM Intersecting a Horizontal Fracture

The flow domain for a perpendicular intersection between the fracture plane and the FRPFM axis is depicted in Figure 3. The fracture is considered a horizontal planar two dimensional flow domain Γ_1, which is geometrically and hydraulically coupled along a circumference *ABCD* to another two dimensional flow domain Γ_2 consisting of the curved cylindrical FRPFM surface (mesh plus sorbent plus external visual indicator fabric) of radius r_0 [L] and thickness $H \ll r_0$ [L]. Both the fracture and the FRPFM surface layer are relatively thin with respect to the FRPFM diameter and are idealized as homogeneous and isotropic sheets (conceptually zero thickness) of known effective transmissivities T_1 and T_2 [L^2/T]. These transmissivities represent fracture aperture and FRPFM layer thickness multiplied by the respective hydraulic conductivities. Far from the FRPFM location, the fracture plane is assumed to contain a uniform and fracture aperture integrated groundwater flux q_0 [L^2/T], which is equivalent to a fracture discharge per fracture transverse length. Based on these assumptions a flow field solution is presented in Appendix A. To facilitate visualization, the FRPFM surface Γ_2 may be unrolled as in Figure 4 showing the streamlines of intercepted flow inside the sorbent layer (black) with flow directions indicated by blue arrows.

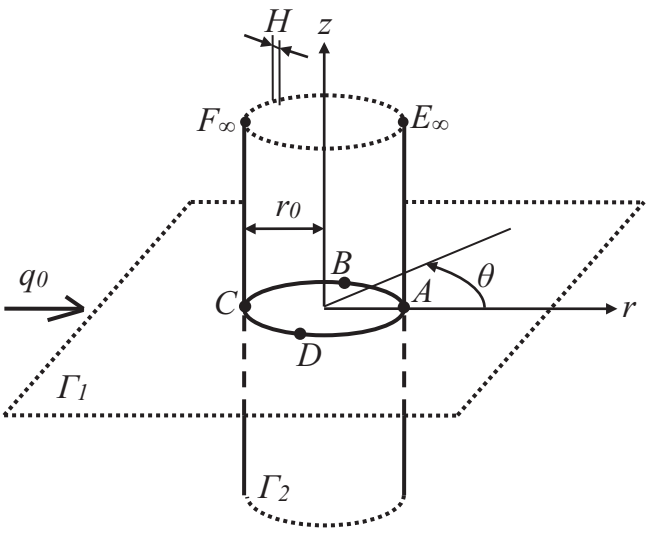

Figure 3. Flow domains Γ_1 (fracture plane) and Γ_2 (FRPFM surface) connected along circumference *ABCD* (example of perpendicular intersection).

With other PFM designs [e.g., *Hatfield et al.*, 2004] it has been appropriate to model tracer elution from a sorbent material to quantify groundwater flux; whereas, contaminant sorption onto that same sorbent or another is used to estimate contaminant flux [*Stucker et al.*, 2011]. In both cases, sorption is typically modeled as piecewise linear, instantaneous, and advection driven. For purely advective transport in combination with linear and instantaneous sorption, the

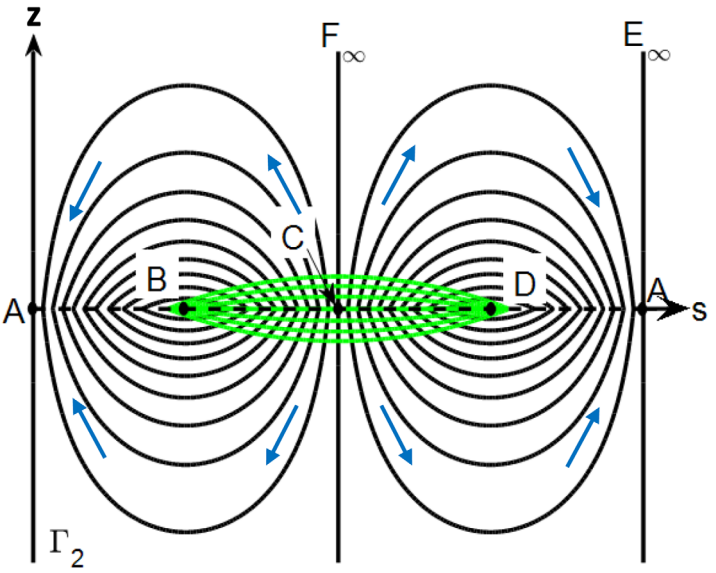

Figure 4. Unrolled (flat) domain of Γ_2 showing the streamlines (black with blue arrows indicating flow direction) and tracer or contaminant isochrones (green) as derived in Appendix A. The isochrones represent the retreating front of dye or tracer eluted under an intercepted cumulative groundwater flux, or the leading front of a contaminant captured from that same intercepted volume of groundwater.

stream tube based method of *Klammler et al.* [2009] is applied to the FRPFM configuration as shown in Appendix A. The green lines in Figure 4 represent a transient sequence of isochrones illustrating the retreating front of dye or tracer, which are advectively eluted under an intercepted cumulative groundwater flux. Alternatively, the isochrones may be interpreted as the temporal advancement of the leading front of a contaminant captured from that same intercepted volume of groundwater (cumulative contaminant flux).

4. Water Flux Estimation

The isochrones in Figure 4 delimit areas in Γ_2 depleted of dye or tracer, which increase with the cumulative volume of groundwater intercepted by the FRPFM. As shown in Appendix A, a dimensionless dye mark size $m_{out} = A_{dye}/r_0^2$ [−] may be defined and related to a dimensionless travel time τ [−] according to the bold continuous line in Figure 5. With this, an observed dye mark area A_{dye} [L^2] may be used to estimate τ and the undisturbed fracture flux q_0 from

$$q_0 = \frac{2HnRr_0\tau}{\alpha t} \tag{1}$$

where R [−] is the retardation factor of the dye, n [−] is the compound sorbent layer porosity, and t [T] is time of exposure. The parameter α [−] accounts for the distortion of the uniform ambient flow field in the vicinity of the FRPFM and is given by

$$\alpha = \frac{2}{1+\frac{T_1}{2T_2}} \tag{2}$$

as again argued in Appendix A. As an alternative to a graphical reading from Figure 5, the following approximations apply

$$\tau \approx m_{out}\left(5.3\cdot 10^{-4}m_{out}^2 + 1.8\cdot 10^{-4}m_{out} + 0.25\right) \approx \frac{m_{out}}{4} \tag{3}$$

The first approximation is based on a least squares fit and visually indistinguishable over the range depicted. The second approximation is a linear fit at the origin (bold dotted line). It is derived in Appendix A and highly accurate up to $m_{out} \approx 7$. In physical terms, the linear approximation assumes that each elementary volume of groundwater entering the sorbent layer elutes the same amount of dye or tracer from the device at all times (i.e., no stream tube through the sorbent layer becomes completely empty of dye or tracer). This is a desirable condition for practice, as sensitivity to groundwater flow remains at its maximum, corresponding to the steepest portion of the graph in Figure 5. For an unknown groundwater flux in a fracture and a prescribed FRPFM deployment period, this desirable condition may be established by providing a suite of tracers on the sorbent layer with a large enough range of retardation factors. The goal is that at least one tracer yields results in the linear and most sensitive range for flux estimation.

In lieu of measuring A_{dye}, the maximum vertical distance Δz_{dye} between dye isochrones above and below the fracture can be measured, which occurs at point location C in Γ_2 (see Figure 4). As derived in Appendix A, Δz_{dye} is related to τ by

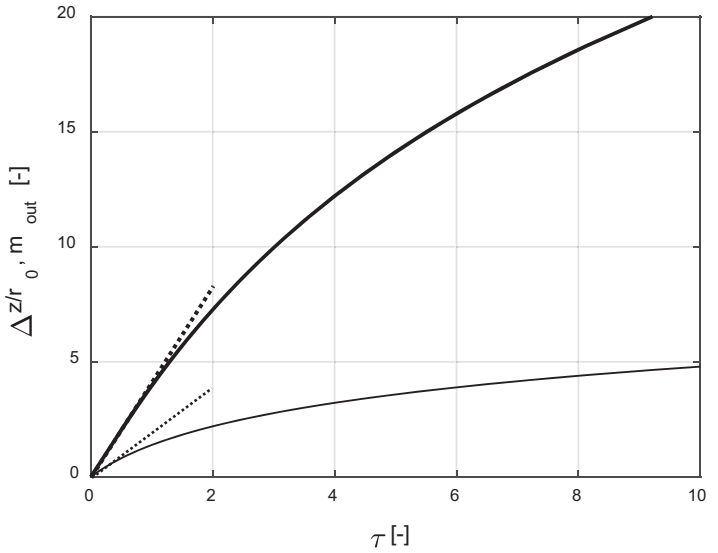

Figure 5. Dimensionless dye or tracer loss m_{out} (bold continuous) and dimensionless dye mark width $\Delta z_{dye}/r_0$ (thin continuous) as functions of dimensionless travel time τ. Dashed lines are linear approximations at the origin.

$$\tau = e^{\frac{\Delta z_{dye}}{2r_0}} - 1 \approx \frac{\Delta z_{dye}}{2r_0} \quad (4)$$

which is represented by the thin continuous line in Figure 5. With τ from Figure 5 or equation (4), equation (1) again delivers q_0. The approximation is derived from a linear fit to the graph at the origin (thin dotted line) and accurate for $\Delta z_{dye}/r_0 < 1$. Similar to m_{out}, this is the range where Δz_{dye} is most sensitive to groundwater flux; moreover, the dye mark is still confined enough above and below the fracture intersection to facilitate reliable inference of fracture location, orientation, and flow direction. In practice, the desirable conditions of $\Delta z_{dye}/r_0 < 1$ (while still observing visual dye marks) may be achieved by selecting deployment time and dye retardation based on a preliminary (order of magnitude) estimate of groundwater flux in the fracture.

In the case of soluble tracer loss, Figure 5 or equation (3) can again be used; however, this time $m_{out} = M_{out}/(C_t r_0^2)$, where M_{out} [M] and C_t [M/L^2] are the tracer mass lost and initial tracer concentration per unit sorbent area, respectively. Equation (1) also remains applicable by using the retardation factor R of a tracer. In practice, m_{out} for soluble tracers is determined by laboratory analysis for cylindrical sample strips of the sorbent of finite width w [L] (in vertical direction), which is assumed to be centered about the fracture intersection. The width of the sample strip with respect to the maximum vertical tracer front separation distance Δz_{tra} [L] is critical. As long as $w > \Delta z_{tra}$, it is the case that tracer loss is entirely contained in the sampling strip and changes in w do not affect m_{out}. However, choosing w very large may lead to a reduced sensitivity to the actual amount of tracer lost near the fracture. In contrast, for small values of w (i.e., $w < \Delta z_{tra}$), an increasing portion of the additional tracer loss occurs outside the strip and is not perceived. Based on this, an optimal relative sample strip width is proposed as being only slightly larger than Δz_{tra}. Using the visually observed Δz_{dye} from a dye of retardation R_{dye}, equations (1) and (4) can be used to show that Δz_{tra} for a tracer of retardation R_{tra} may be found from

$$\Delta z_{tra} = 2r_0 \ln\left\{1 + \frac{R_{dye}}{R_{tra}}\left[\exp\left(\frac{\Delta z_{dye}}{2r_0}\right) - 1\right]\right\} \approx \frac{R_{dye}}{R_{tra}}\Delta z_{dye} \quad (5)$$

Figure 5 and equation (3) are valid for $w > \Delta z_{tra}$. In practice, this condition may be verified by consecutively sampling strips away from the fracture intersection and observing no more tracer loss beyond a certain distance from the intersection (which would be approximately equal to $\Delta z_{tra}/2$). While equation (5) still gives a useful idea about the necessary geometric extend of AC felt sampling, the consecutive sampling of smaller strips (and adding detected tracer losses from all strips) is applied in the experimental study below.

5. Contaminant Flux Estimation

Figure 5 and equation (3) are also valid for the accumulation of target contaminants on the sorbent, if $m_{out} = M_c/(r_0^2 H n R_c C_c)$ is used, where M_c [M] is the mass of contaminant detected in the sorbent and the denominator represents the sorption potential for the contaminant on a sorbent of area r_0^2. Hereby, R_c [−] denotes the contaminant retardation factor and C_c [M/L^3] denotes the average concentration in the sorbent pore water, being representative of the flux average concentration in intercepted groundwater. While R_c is known or may be determined, once a contaminant is identified, C_c is generally unknown. However, knowing

q_0 from tracer data as discussed above, equation (1) may be inverted to express a dimensionless travel time τ for a contaminant as

$$\tau = \frac{q_0 \alpha t}{2HnR_c r_0} \approx \frac{M_c}{4HnR_c r_0^2 C_c} \tag{6}$$

where the approximation is based on $\tau \approx m_{out}/4$ from equation (3) for small values of τ. The product $q_0\alpha$ in equation (6) represents the water discharge per transverse length captured by the FRPFM sorbent. Division by $2Hn$ yields the corresponding pore velocity of water for uniform flow through the sorbent of total thickness $2H$ (above and below fracture; as in fictitious flow domain Γ_3 in Figure A2). Further division by R_c yields the velocity of contaminant transport, such that τ may be interpreted as the physical time t, normalized to the time a contaminant particle takes to travel a distance r_0 in uniform flow through the sorbent layer. An analogous interpretation applies to τ in equation (1) for tracer elution and respective retardation factors. Knowing τ from the exact equality in equation (6), Figure 5 provides a corresponding value of m_{out}, which delivers $C_c = M_c/(r_0^2 HnR_c m_{out})$ and the ambient contaminant mass flux is obtained as $J = q_0 C_c$ [M/(LT)] (again defined as mass flow per unit transverse fracture length or as fracture width integrated flow).

However, the appropriate choice of a sorbent material should generally assure strong contaminant sorption ($R_c \gg 1$). This translates into small values of τ and the approximate equality in equation (6) becomes valid for substitution in equation (1) after multiplication by C_c to convert q_0 into J. This results in a simplified estimate of

$$J \approx \frac{M_c}{2r_0 \alpha t} \tag{7}$$

which is independent of both R_c and C_c. It may be interpreted as the contaminant mass crossing a borehole diameter per unit time, after correcting for local flow distortion by α (i.e., in the undisturbed ambient flow field). The approximations taken to obtain equation (7) imply that no contaminant particle previously sorbed is again released from the sorbent, which is expected to be highly accurate in practice, where sorbents are selected to fully retain target contaminants. Moreover, given the approximations of equations (1) and (7) are accurate, dividing equation (7) by equation (1) yields an estimate of the flux averaged contaminant concentration C_c as

$$C_c \approx \frac{M_c}{HnR_{tr} r_0^2 m_{out,tr}} \tag{8}$$

where the additional subscript "tr" with R and m_{out} is used to clarify that these variables describe properties of a tracer (or dye). Besides avoiding problems with contaminant mixing in borehole or monitoring well, equation (8) illustrates that estimates of C_c from the FRPFM do not depend on the potentially uncertain flow convergence parameter α, nor the particular value of contaminant retardation R_c (it just needs to be large enough to rule out desorption).

6. Materials and Experimental Design

Laboratory experiments were conducted to evaluate the FRPFM in a "simulated" rock well intersected by a single horizontal fracture, such that measurements of cumulative water and contaminant fluxes could be made under controlled conditions. Shown in Figure 6 is the apparatus for simulating fracture flow ("fracture flow apparatus") constructed with two sections of clear PVC pipe (10.2 cm inner diameter) and two acrylic sheets (27 cm × 53 cm × 1.2 cm). The PVC pipes are aligned with 10.2 cm diameter holes centered on each sheet. The top acrylic sheet was fastened on top of the bottom sheet using incompressible rubber spacers to maintain a uniform fracture aperture of 500 μm between the sheets. The completed system simulates a borehole intersecting a horizontal planar fracture. The outer perimeter of the fracture plane was sealed using a compressible rubber gasket. There was one inlet and one outlet port located on the bottom sheet of acrylic in order to establish flow along the plane. Both the inlet (up-gradient) and effluent (down-gradient) ports were connected to a channel etched into the inner face of the acrylic creating a constant head boundary at either end of the flow system. A Marriotte (aspirator) bottle was connected to the influent line in order to maintain constant pressure at the up-gradient (influent) port. Flow through the system was controlled by adjusting the elevation of the effluent end of the down-gradient tube relative to the Marriotte

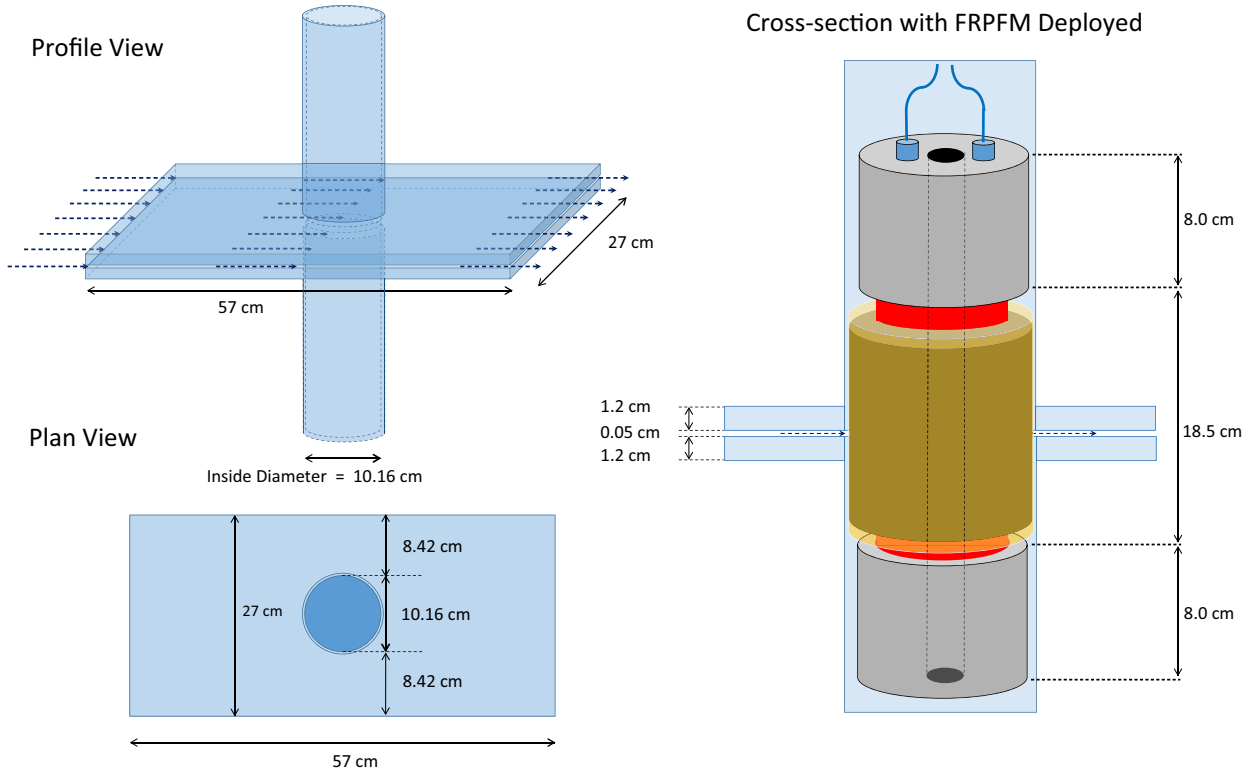

Figure 6. Fracture flow apparatus with FRPFM prototype deployed. Horizontal fracture of aperture 500 μm, width 27 cm, length 53 cm, and hydraulic transmissivity 8.8 m^2/d; borehole diameter 10.2 cm.

bottle, creating a constant head differential across the system and inducing flow proportional to the resulting hydraulic gradient.

The outer layer of the FRPFM core consisted of an elastic fabric (nylon/spandex blend, 95% nylon and 5% spandex; part number 10655272, Jo-Ann Fabric & Craft, OH, USA) pre-treated with a water soluble dye for a visual indication of flow through the device. To prepare the visual dye fabric, 60 mL of Turmeric was simmered in two liters of water for 1–2 hours and then allowed to cool. The dissolved dye was then transferred to a reservoir containing the fabric. The reservoir was slowly agitated for 12 hours before the dyed fabric material was removed, drained, and used to construct the FRPFM.

The inner layer of sorbent material was activated carbon felt (AC Felt 1300; part number MY-QW-01, Ameriasia Advanced Activated Carbon Products Co., Ltd., Nantong, China), that was 0.25 cm thick and had a porosity and dry bulk density of 0.92 and 0.075 g/cm^3, respectively. 1-butanol, 2-butanol, 1-pentanol, 3-pentanol, 1-octanol, and 1-heptanol served as resident tracers pre-equilibrated on the AC felt. Pre-equilibration involved the use of acetone spiked with the tracers (750 mg/L for 1-butanol, 2-butanol, 1-pentanol, 3-pentanol; 400 mg/L for 1-heptanol; 200 mg/L for 1-octanol). Two pieces of AC felt (each 30 cm by 15.5 cm) were placed in a 2 L glass jar with 1.7 L of acetone tracer solution. The jar was slowly shaken over 12 hours to generate a uniform tracer distribution on the AC felt. The acetone-wet felt was placed on a stainless screen rack in a laboratory exhaust hood for 1 hour to promote acetone volatilization. After drying, the felt was used for FRPFM assembly.

The FRPFM assembly and installation involved the following steps: First, the inflatable core packer was wrapped with nylon mesh (Poly-Net^{TM} Protective Netting, HDPE, Cole Parmer) to a thickness of 0.5 cm. The mesh had a porosity of 0.81 and was highly permeable. Its purpose was to facilitate flow through the compound layer of mesh, AC felt and dye fabric. Then two pieces of tracer preloaded AC felts were wetted with solute/tracer free water and carefully placed and wrapped over the mesh layer. The final assembly procedure was to emplace the Turmeric dyed sewn elastic fabric socks (nylon/spandex blend, 30 cm long and 22 cm circumference) over the AC felt layer. The porosity and felt carbon density of the combined mesh-felt-fabric layer were $n = 0.83$ and $\rho = 0.028$ g/cm^3, respectively.

During each FRPFM test, the Marriotte bottle was filled with aqueous source solution containing a surrogate contaminant (14–16 mg/L 2-octanol). Prior to FRPFM installation, the entire fracture flow apparatus was flushed with source water to achieve a uniform 2-octanol concentration in the fracture plane and borehole system. The assembled FRPFM was then inserted into the simulator borehole and centered over the fracture. Next, the core packer was inflated, followed by the upper and lower packers. Finally, valves to the Marriotte bottle and the effluent reservoir flow were opened to initiate flow under a prescribed head gradient and to create a desired discharge through the fracture.

After a specified period (ranging from 1 to 16 days in our experiments), the valves connecting the Marriotte bottle and the effluent line to the fracture simulator were closed, and the end packers were deflated before the FRPFM core. The FRPFM was immediately retrieved from the well and the cumulative volume of collected effluent was measured. The FRPFM was placed under a UV-light in a dark room where pictures were taken of the external FRPFM layer to record indications of flow in the fracture through the FRPFM produced by the dye. The external layer was removed and the inner layer sorbent (AC felt) was sampled in circumferential strips. Regular intervals of 0.4–0.5 cm in axial (vertical) length of the AC felt were segmented and transferred to 40 mL VOA vials with Teflon-lined septa caps containing an extraction fluid (acetone or methylene chloride). Each strip of sampled AC felt was extracted using 30 mL of solvent. Sample vials were rotated at low speed for 24 hours, and then allowed to settle at room temperature (21°C ± 1°C) for 6 hours. The supernatant was sub-sampled in 2 mL GC vials for GC analysis. A syringe filter (Cameo 17F syringe filter, Teflon, 0.22 μm) was used to filter samples for particulates. The samples were analyzed for alcohol tracers and surrogate contaminant (2-octanol) by GC flame-ionization detector (FID). The GC column used was a 105 m × 0.53 mm, 3 μm fixed phase, Rtx-624 column (temperature limits: −20°C to 240°C). Sub-sampling, filtering and GC-analysis took approximately 80 min per sample strip.

7. Hydraulic Characterization of the Fracture Flow Apparatus and Tracer Elution Experiments

The hydraulic transmissivity T_1 of the fracture plane is estimated by the cubic law [Hele Shaw analogue; *Strack*, 1989] as $T_1 = \rho g e^3/(12\mu) = 8.8$ m^2/d, where $\rho = 10^3$ kg/m^3 and $\mu = 10^{-3}$ kg/(ms) are density and dynamic viscosity of water, $g = 9.8$ m/s^2 is acceleration of gravity and $e = 0.5$ mm is fracture aperture. The solution to the potential flow problem in Figure A2 assumes a theoretically infinite flow domain Γ_1. To investigate the experimental artifact resulting from the finite dimension of the apparatus and, hence, Γ_1, a series of numerical flow simulations was conducted using a single layer MODFLOW model using $2T_2/T_1 = 0.01$, 0.1, 0.2, 0.5, 1, 2, 5, 10, 100 and 1000. Figure 7 represents the flow field obtained for open borehole conditions approximated by $2T_2/T_1 = 1000$. Simulation results in terms of $\alpha = q_1/q_0$ as a function of $2T_2/T_1$ are represented by the circles in the Figure 8. The maximum assumed value for $2T_2/T_1 = 1000$ produces $\alpha = 1.76$, which is smaller than the theoretical value of 2 from the convergence equation for an infinite flow domain given by equation (2) and the continuous line. This is a reflection of the fact that the nearby boundaries reduce flow convergence towards the well. However, equation (9) as represented by the stars in Figure 8 (which nicely coincide with the circles) could be found as an empirical approximation for α given the finite dimensions of the fracture flow apparatus.

$$\alpha = \frac{2.23}{1+\frac{T_1}{2T_2}} - \frac{0.47}{\left(1+\frac{T_1}{2T_2}\right)^2} \tag{9}$$

For additional validation of the numerical results and equation (9), multiple borehole dilution tests in packered-off sections of the borehole containing the fracture intersection were conducted under a range of constant flow conditions. Figure 9 shows a typical result of observed changes in electrical conductivity with respect to time for a given flow rate in the fracture. Figure 10 summarizes results for different flow rates and successfully validates the flow convergence derived from the numerical model (Figure 8) and equation (9) for the case of $2T_2/T_1 \gg 1$, i.e., applying $\alpha = 1.76$.

A series of dynamic tracer elution tests were conducted with AC felt to characterize the elution behavior of resident tracers with regard to cumulative water flow and to estimate linear tracer-carbon sorption coefficients for each resident tracer. Columns of 1.5 cm inner diameter and 5 cm length were wet-packed with the tracers preloaded on AC felt. The packed columns were flushed with steady water flow at 0.5–2.5 mL/min to effect

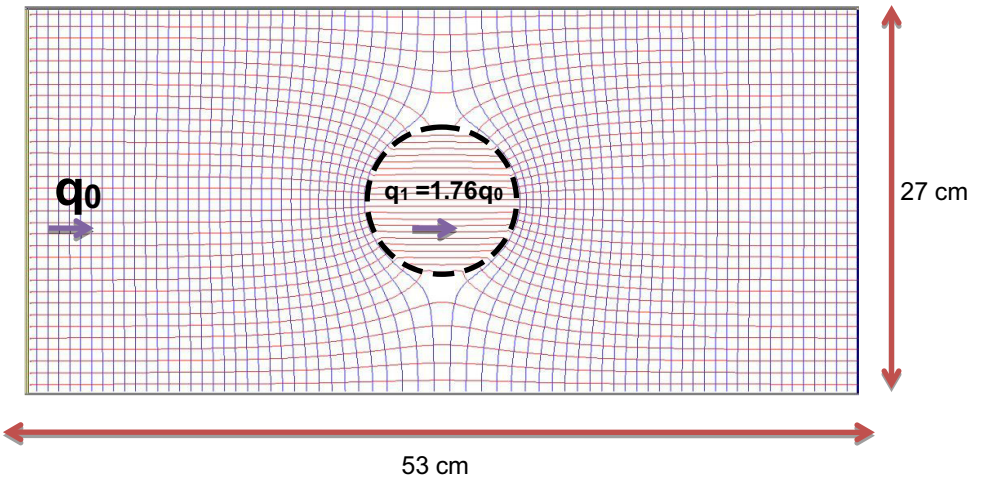

Figure 7. MODFLOW simulated stream lines (red, essentially from left to right) and potential lines (blue, essentially from top down) for the fracture flow apparatus under open borehole conditions ($2T_2/T_1 = 1000$). The circular flow domain Γ_3 containing uniform flow is used in the mathematical derivation and does not exist in the physical FRPFM setup.

tracer elution. After a specific period of water flow, the AC felt was removed from the column to quantify the mass of all resident tracers remaining. Several column tests were conducted to cover a range of flow conditions and durations. The retardation factor R_{elu} of each tracer for the AC felt was estimated from the slope of the linear portion of each tracer's elution function (*Hatfield et al.*, 2004). Figure 11 shows the relative mass m_r [−] of tracer retained on AC felt versus cumulative elution pore volume normalized with respect to R_{elu}. Pertinent values of R_{elu} and resultant sorption coefficients K_p for AC felt are summarized in Table 1 in conjunction with a conversion to retardation factors R for the compound AC felt and mesh layer.

Resident tracers 1-octanol and 1-heptanol possess aqueous to activated-carbon retardation factors in excess of 10,000; thus, they functionally behave as nondesorbing resident tracers compared to 1-butanol, 2-butanol, 1-pentanol, and 3-pentanol. As such, 1-octanol and 1-heptanol were used as internal standards in the sense that m_{out} for 1-butanol, 2-butanol, 1-pentanol, and 3-pentanol were assessed from measured changes in initial tracer mass ratios with respect to 1-octanol and 1-heptanol [*Hatfield et al.*, 2004]. The retardation factor R of the dye was not measured independently, but inferred from a least squared fit of estimated fracture fluxes from dye mark width measurements (Δz_{dye}) and true fracture fluxes through the apparatus.

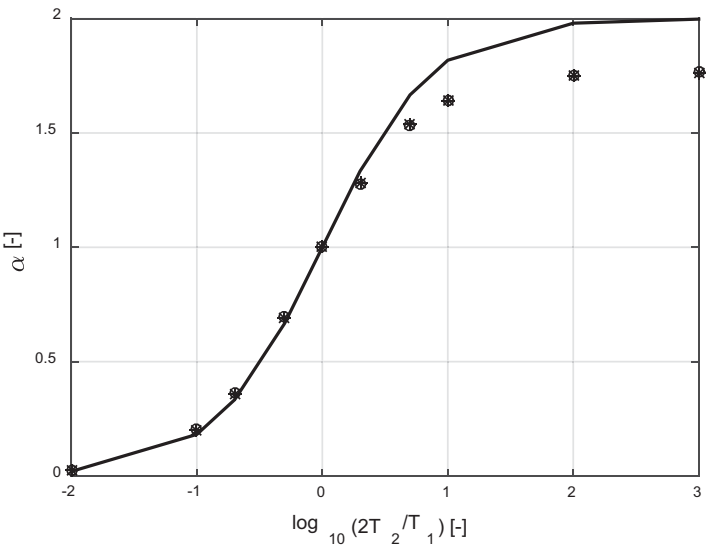

Figure 8. Flow convergence factor α as a function of $2T_2/T_1$ from equation (2) for infinite flow domains (continuous line), from MODFLOW simulation for the finite dimensions of the fracture flow apparatus (circles), and from approximate equation (9) (stars coinciding with circles).

8. Results

Figure 12 shows photographs of the outer dye fabric of a FRPFM after retrieval from the fracture flow apparatus. It is seen that the dye was displaced along the up-gradient portion of the FRPFM circumference with the largest vertical dye front displacement Δz_{dye} occurring near point *C*. Comparison with the dye fronts (green isochrones) depicted in Figure 4 shows very good agreement

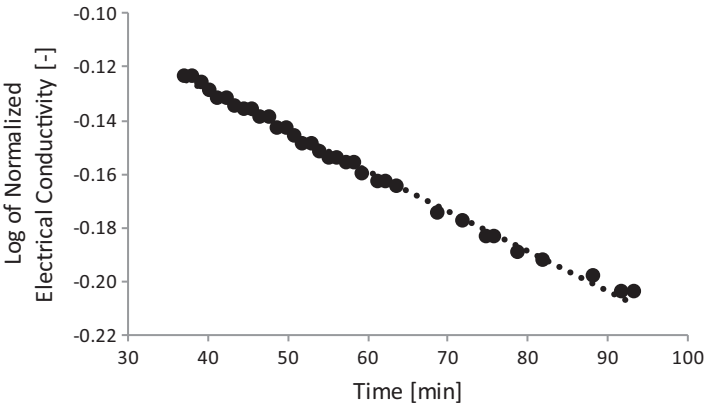

Figure 9. Typical result from a borehole dilution test conducted in the fracture flow apparatus showing changes in observed electrical conductivity with respect to time for a given flow rate in the fracture.

with the theoretical model. Thus, Figure 12 supports the theoretical model adopted in qualitative terms of dye mark shape and demonstrates that the FRPFM allows for visual identification of the location and orientation of hydraulically active fractures as well as the direction of flow inside the fracture. Moreover, but not shown here, the dye marks from different experiments confirm the theoretical result that, with increasing cumulative water flow, the size of the dye marks grows more rapidly in the vertical direction, whereas it barely changes in the circumferential direction. This is also in qualitative agreement with the sequence of green isochrones in Figure 4.

For a quantitative validation of results, we apply the equations presented above to estimate cumulative water and contaminant fluxes for comparison to known true fluxes imposed through the fracture flow apparatus. Table 2 summarizes the relevant physical parameters. As an example, we take an experiment, which was run for $t = 1$ d conveying a total flow volume of $V = 2460$ cm^3 with contaminant concentration $C = 0.015$ mg/cm^3 through the fracture flow apparatus. Knowing from Figure 6 that the width of the fracture is 27 cm, this translates into true cumulative water and contaminant fluxes (or discharges per unit fracture width perpendicular to flow) of $q_0t = 2460/27 = 91$ cm^2 and $Jt = 2460{\cdot}0.015/27 = 1.3$ mg/cm, respectively. The corresponding measurements delivered by the FRPFM were dye mark width $\Delta z_{dye} = 0.15$ cm, relative 1-pentanol mass lost $m_{out} = 0.13$ and contaminant mass sorbed $M_c = 3.2$ mg. Substituting equation (4) into equation (1) with the parameters of Tables 1 and 2 yields an estimate of $q_0t = 0.66{\cdot}0.83{\cdot}330{\cdot}0.15/0.28 = 97$ cm^2 based on dye mark width. Substituting equation (3) into equation (1) gives an estimate of $q_0t = 0.66{\cdot}0.83{\cdot}182{\cdot}5.1{\cdot}0.13/(2{\cdot}0.28) = 117$ cm^2 based on invisible tracer loss. Equations (7) and (8) deliver estimates of cumulative contaminant mass flux $Jt = 3.2/(2{\cdot}5.1{\cdot}0.28) = 1.1$ mg/cm and flux averaged contaminant concentration $C_c = 0.010$ mg/cm^3. Figures 13–15 graphically summarize results of different experiments and serve as a quantitative validation of the FRPFM performance. The regression lines shown are forced to zero intercept and relative errors on estimated water and contaminant fluxes are 2% ± 25% and −2% ± 16% (mean ± one standard deviation), respectively. Results shown for alcohol tracers are averages computed from estimates based on 1-pentanol and 3-pentanol, since losses of 1-butanol and 2-butanol were mostly beyond the interval covered by the sampling strips (equation (5)).

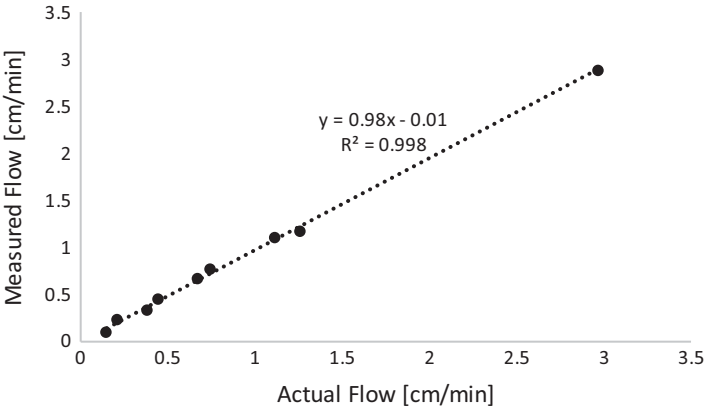

Figure 10. Measured versus actual flow rates in the fracture from multiple borehole dilution tests (for $2T_2/T_1 \gg 1$, i.e., applying $\alpha = 1.76$ from equation (9) or Figure 8).

The computation of M_c and m_{out} accounts for the effects of insertion/removal of the FRPFM into the borehole as well as of FRPFM inflation. The former is considered by using the average tracer and contaminant concentrations of the outermost sampling strips as a reference for computing contaminant sorption and tracer loss due to fracture flow from the inner sampling strips closer to the fracture. Observing dye mark widths up to approximately

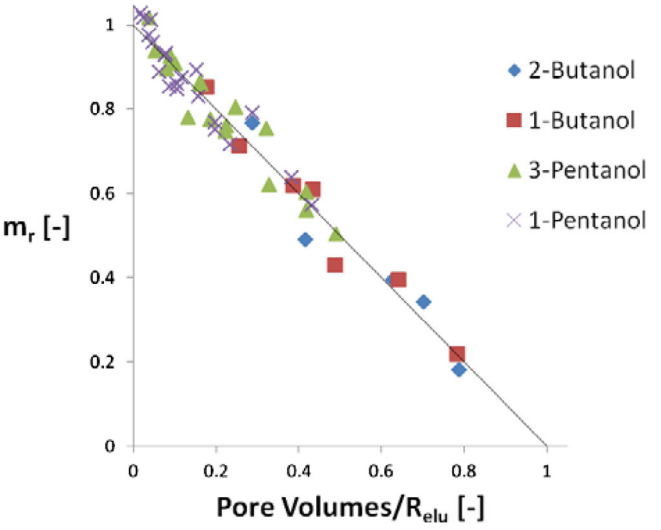

Figure 11. Data from the linear portion of each resident tracer's elution curve for AC felt flushed with water. Relative residual tracer mass m_r for each tracer is plotted against the number of pore volumes of water flushed through the column after normalization to a tracer's retardation factor R_{elu} (*Hatfield et al.*, 2004).

0.5 cm in our experiments, this is justified by equation (5) for the pentanol tracers. During inflation of the core packer, a volume of approximately 300 mL (corresponding to the ring volume between deflated packer and borehole wall over the vertical length of the sampling interval) has to be displaced from the borehole in the up and downward directions. Knowing the contaminant concentration, the respective contaminant mass sorbed during inflation is subtracted to find M_c used in estimation of contaminant discharge above. Similarly, the values of m_{out} are obtained by subtracting the amount of tracer loss due to the same volume of water displaced during inflation. We recognize, that this type of correction is not viable in field situations. Possible alternatives include the deployment of a physical "shield" protecting the sorbent layer during installation and removal in a borehole, or the performance of additional "push-pull" tests, where all installation and removal steps are performed without leaving the device in place (no exposure to groundwater flow). Similar effects are also likely to occur with the visible tracer. However, changes in the background color are uniform or too gradual to be observed, such that the sharp-cut fronts of dye displacement can still be clearly identified by visual inspection or means of digital image processing on photographs.

All parameters needed for computation of flux estimates were independently measured or estimated, except for flow convergence factor α and dye retardation factor R_{dye}, which were estimated from FRPFM results. In particular, instead of independently measuring the compound sorbent layer transmissivity T_2 to estimate α from equation (9), α was used as a fitting parameter to minimize the average bias in water and contaminant flux estimates based on m_{out} and M_c. That is, $\alpha = 0.28$ was chosen as the value, which brings the regression slopes in Figures 14 and 15 as close to one as possible. By equation (9) with $T_1 = 8.8$ m^2/d (Table 2), this translates into an estimate of $T_2 = 0.66$ m^2/d, which serves as a reference value of future FRPFM field deployments. Knowing α, $R_{dye} = 330$ was estimated as the value, which brings the regression slope in Figure 13 to unity (within rounding errors). This value also serves as a reference for future FRPFM deployments using turmeric as a dye.

For field situations, the estimated value of T_2 is used in equation (2) to find α. This, however, also requires knowledge of the highly uncertain fracture transmissivity T_1 (unless $T_1 \ll 2T_2$ is the case, such that $\alpha \approx 2$). Combining FRPFM with other hydraulic or geophysical borehole methods may prove valuable for overcoming this challenge by gaining independent information on T_1 either directly or through measurements of fracture aperture and application of the cubic law. Notwithstanding uncertainty in α, the linear

Table 1. Tracer and Dye Retardation Factors R for the Compound Sorbent Layer Including Mesh, AC Felt, and Dye Fabric

	2-Butanol	1-Butanol	3-Pentanol	1-Pentanol	Turmeric (dye)
R_{elu}	24	37	175	433	–
K_p[a] (cm^3/g)	282	503	2134	5300	–
R[b]	11	16	74	182	330[c]

R_{elu} and K_p are retardation factors and sorption coefficients of AC felt alone as estimated from tracer elution experiments.
[a]From the retardation factor R_{elu} of each tracer estimated from elution experiments using AC felt alone, and using felt properties of 0.92 porosity and 0.075 g carbon/cm^3.
[b]Tracer retardation factors for the combined AC felt and mesh layer using effective properties of $n = 0.83$ porosity, $\rho = 0.028$ g carbon/cm^3 and the above listed tracer sorption coefficient K_p.
[c]From a least squares fit of estimated versus true water discharge through the fracture flow apparatus (Figure 13).

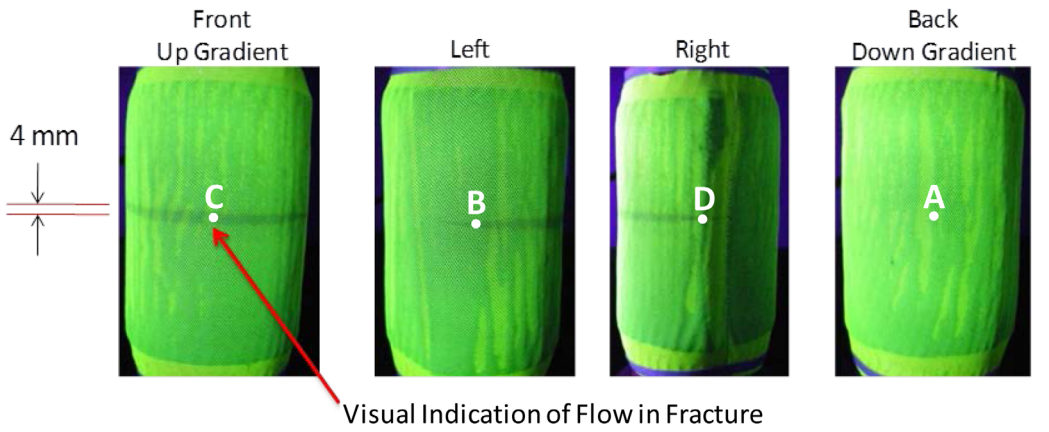

Figure 12. Visual identification of flowing fracture and flow direction by dye mark on the external FRPFM sock. White dots and letters are for comparison to theoretical dye fronts shown as green lines in Figure 4.

approximation of equation (3) remains valid, even if the flow field in the sorbent layer deviates from that of the theoretical model (e.g., due to irregularities in the borehole wall, heterogeneities in the FRPFM layer, or nearby packers). This is true for short enough times (approximately $\tau < 2$ from Figure 5), such that each elementary volume of water intercepted by the FRPFM elutes the same amount of tracer(s), regardless of the exact flow paths through the sorbent (no stream tubes completely empty of tracer). The same applies to contaminant sorption; as long as it is assured that none of the contaminant sorbed is again released from the device, equation (7) remains valid (no stream tubes completely saturated with contaminant). Under the conditions of linear tracer elution and contaminant sorption, it is further the case that contaminant concentrations estimated from dividing contaminant mass fluxes by water fluxes become independent of α and, hence, the uncertainties associated with it. Intuitively speaking, this is the case, because concentration measurements do not depend on the amount of water sampled (under homogeneous conditions).

Furthermore, in practice, fractures do generally not intersect the borehole perpendicularly, nor do they occur isolated and infinitely distant from the impermeable top and bottom packers. These issues are given some theoretical attention in Appendices B and C in terms of generalized flow convergence factors, which may be used in equations (1) and (7) instead of α. It is seen that the influence of fracture inclination (dip angle) also depends on the incident flow direction in the fracture as well as the transmissivity contrast T_1/T_2 between fracture and sorbent layer. Regardless of those parameters, however, it if found that the relative impact on water and contaminant flux estimates can be positive or negative, but is less than approximately 20% for fracture inclinations up to 30° (Figure B3). With regard to nearby horizontal fractures or a single horizontal fracture centered between nearby packers, it is found that the relative impact is always negative (smaller flow intercepted) and less than approximately 20% for fracture or packer separation distances down to approximately $2r_0$ (Figure C1). In the same way as discussed in Section 5, estimates of flux averaged contaminant concentrations from equation (8) are not affected by fracture inclination or nearby boundaries.

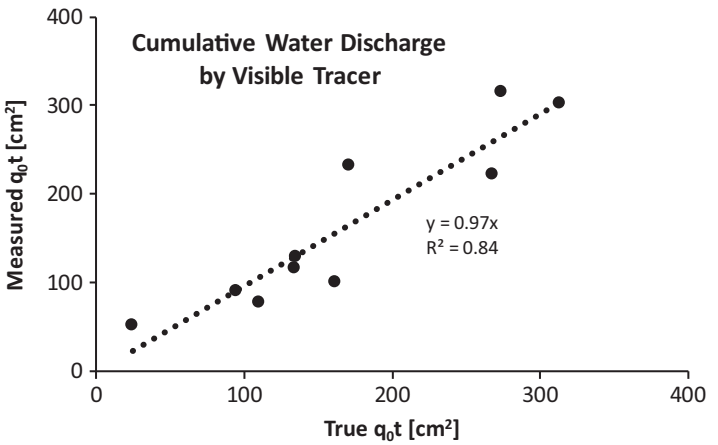

Figure 13. Measured cumulative water fluxes by FRPFM visible tracers (using dye mark width Δz_{dye} in equations (1) and (4)) versus controlled cumulative discharge in fracture flow apparatus.

9. Summary

The objective of the current study was to develop the

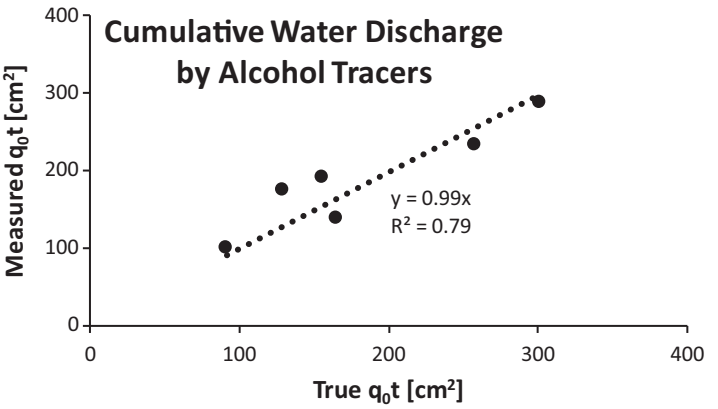

Figure 14. Measured cumulative water discharge by FRPFM alcohol tracers (using relative tracer loss m_{out} in equations (1) and (3)) versus controlled cumulative discharge in the fracture flow apparatus.

fractured rock passive flux meter (FRPFM) as new technology that directly measures fracture specific magnitudes and directions of cumulative water and contaminant fluxes in fractured media. The FRPFM functions like an inflatable (or mechanically expandable) packer that lines the borehole, while holding two reactive permeable fabrics against the wall of the borehole and to any water-filled fractures intersected by the borehole. The first outer layer constitutes an elastic (nylon/spandex blend) fabric sock dyed with turmeric, while an inner reactive layer consists of activated carbon (AC) felt pretreated with a suite of alcohol tracers. Visual inspection of the FRPFM dye marks leads to estimates of the following for hydraulically active ("flowing") fractures: (1) locations along the borehole; (2) number of fractures; (3) individual fracture orientations; and (4) groundwater flow directions and cumulative magnitudes in fractures. Further analytical analysis of the AC felt for masses of tracer remaining and contaminants sorbed at indicated locations of active fractures yield: (5) cumulative magnitude of groundwater flux in fractures; and (6) cumulative magnitude of contaminant mass flux in fractures. The fluxes obtained are fracture width integrated, i.e., flows or (mass) discharges per fracture length perpendicular to flow direction. The FRPFM does not provide direct indication of fracture aperture as required for estimating flow velocities. However, contaminant concentrations in the fracture water can be directly estimated from dividing contaminant fluxes by water fluxes. This avoids complications related to mixing between fracture and borehole water, which arise when taking water samples from open borehole intervals.

We apply potential flow theory and assume advective stream tube transport for developing the equations required to estimate water and contaminant fluxes from measured dye mark widths, tracer masses lost and contaminant masses sorbed. A laboratory bench-scale apparatus for simulating flow through a fracture was devised to demonstrate the working principle of the FRPFM. The fracture flow apparatus consists of two plexi-glass plates emulating a horizontal fracture of 0.5 mm aperture, over which controlled water and (surrogate) contaminant fluxes can be established. The fracture is intersected by a "borehole" for FRPFM installation and multiple experiments at different flow rates and deployment periods were performed. Complementary experiments investigated the tracer elution characteristics as well as the hydraulic properties of the fracture flow apparatus. The laboratory evaluation of the FRPFM demonstrated that visual data successfully provides active fracture location, orientation and incident flow direction, while the measurement of tracer and contaminant masses on the AC felt leads to good estimates of water and

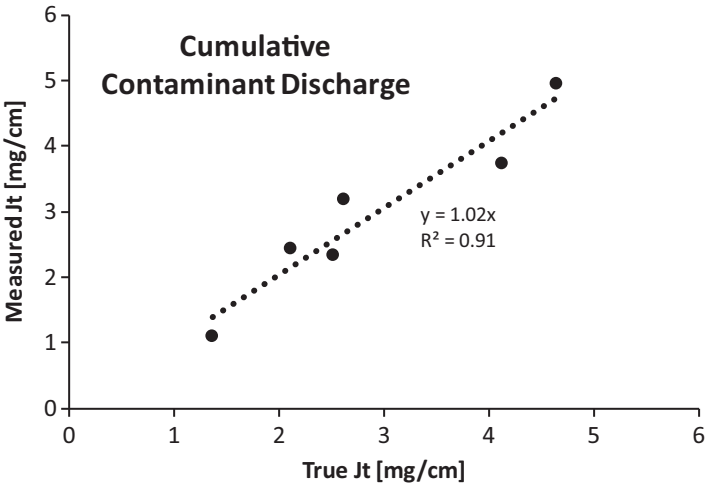

Figure 15. Measured cumulative contaminant discharge by FRPFM (using sorbed contaminant mass M_c in equation (7)) versus controlled cumulative contaminant discharge in the fracture flow apparatus.

Table 2. Parameters Used to Interpret FRPFM Measurements in the Fracture Simulator

r_0	α[a]	H	n	T_1[b]	T_2[c]
5.08 cm	0.28	0.66 cm	0.83	8.8 m^2/d	0.66 m^2/d

[a]From minimizing average error (bias) in water and contaminant flux estimates.
[b]From cubic law.
[c]From equation (9).

contaminant fluxes within approximately 25% of the true values. Simple measurements of dye mark widths are also shown to yield estimates of cumulative water flux within the same range of accuracy. While experiments were performed for a single fracture perpendicularly intersecting a borehole, theoretical generalizations to inclined or multiple horizontal fractures (or nearby impermeable packers) are given.

Appendix A: Flow and Transport Modeling for a Single Perpendicular Intersection

Figures 3 shows the coordinate system adopted with origin at the intersection point of borehole axis z and fracture plane spanned by radial and angular coordinates r and θ. Figure A1 illustrates the unrolled flow domain Γ_2 corresponding to the FRPFM surface, where $s = \theta r_0$ is a coordinate along *ABCD* and $\theta = 0$ is aligned with the incident flow direction of the undisturbed (assumed uniform) flux q_0 in the fracture. The hydraulic coupling of Γ_1 and Γ_2 is achieved by requiring continuity of flow as well as continuity of hydraulic head φ [L] across *ABCD* in Figure 3, while maintaining a uniform far field in Γ_1 (i.e., far from *ABCD*). An example of a well-known solution for a circular inhomogeneity of contrasting conductivity disturbing an otherwise uniform flow field is depicted in Figure A2 (stream lines continuous; potential lines dashed; *Strack*, 1989; *Klammler et al.*, 2007). Based on transmissivities T_1 and T_2, the hydraulic potentials used in Figure A2 are $\Phi_1 = T_1\varphi$ in Γ_1 and $\Phi_3 = 2T_2\varphi$ in Γ_3 [both L^3/T]. This results in the required discontinuity in potential across *ABCD* in order to preserve continuity of φ. The stream function Ψ [L^3/T] is the same in both flow domains and seen to be continuous everywhere. The fictitious (i.e., in the FRPFM problem nonexistent) flow domain Γ_3 inside the circle *ABCD* in the fracture plane is assigned a transmissivity $2T_2$, where the factor 2 anticipates the fact that flow in the fracture will split into two equal parts inside the sorbent (above and below the fracture).

Independent of the transmissivity, however, it is known that Γ_3 contains a uniform flow field, which is of magnitude $q_1 = \alpha q_0$ [L^2/T], where α [−] is a flow convergence factor. For a two-dimensional flow domain of constant thickness and hydraulic conductivities K_1 and K_2 [L/T] outside and inside the circular inhomogeneity, respectively, it is known [*Strack*, 1989; *Klammler et al.*, 2007] that $\alpha = 2K_2/(K_1 + K_2)$. By substituting T_1 for K_1 and $2T_2$ for K_2, which accounts for both contrasting conductivity and thickness of the inhomogeneity, equation (2) in the main text is found.

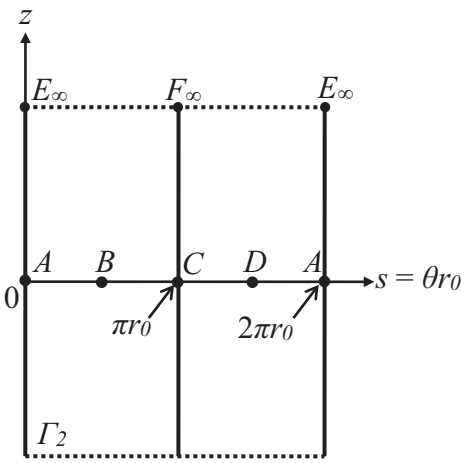

Figure A1. Unrolled (flat) flow domain Γ_2 corresponding to FRPFM surface.

We further define the complex coordinates $\zeta_3 = re^{i\theta}$ within Γ_3 and $\zeta_2 = s + iz$ within Γ_2, where $i = (-1)^{1/2}$ is the imaginary unit. By the rules of conformal mapping [*Strack*, 1989] it is known that the logarithm maps the interior of a circle onto a half strip. Using adequate constants for shifting, scaling and rotation, ζ_2 and ζ_3 as depicted in Figures A1 and A2 can be related by

$$\zeta_2 = -ir_0 \ln \frac{\zeta_3}{r_0} = -ir_0\left(\ln \frac{r}{r_0} + i\theta\right) \tag{A1}$$

Splitting into real and imaginary parts gives

$$s = r_0\theta \tag{A2}$$

$$z = r_0 \ln \frac{r_0}{r} \tag{A3}$$

Since $0 \le \theta \le 2\pi$ and $r \le r_0$, equations (A2) and (A3) confirm that the circular flow domain Γ_3 in

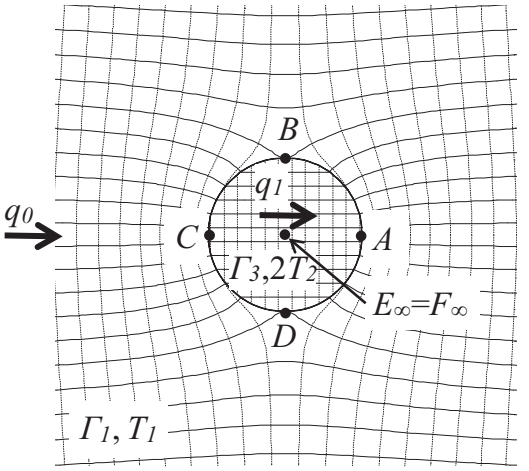

Figure A2. Example of flow field solution for uniform two dimensional flow disturbed by a circular inhomogeneity. The circular flow domain Γ_3 containing uniform flow is used in the mathematical derivation and does not exist in the physical FRPFM setup.

Figure A2 is mapped onto the flow domain Γ_2 consisting of the vertical half-strip in Figure A1 delimited by $0 \le s \le 2\pi r_0$ and $z \ge 0$. Moreover, equation (A2) maps the circumference *ABCD* from Figure 3 to its image in Figure A1 in the exact same way as if the cylindrical FRPFM surface was cut open along AE_∞ and rolled out flat. Thus, equation (A1) may be used to map the known uniform flow field in Γ_3 onto the flow domain Γ_2 resulting in the flow field depicted in Figure 4. This further means that the flow field in Figure 4 may be "cut out" of the piece of paper it is plotted on, rolled up as a cylinder and located on top of *ABCD* in Figure A2 instead of Γ_3, without affecting the flow field in Γ_1. This is because the geometric and hydraulic properties along *ABCD* in Γ_3 and along *ABCD* along the "rolled up" Γ_2 are identical (due to "conformal equivalence" by equation (A1)). Since the flow field in Γ_3 is always uniform, independent of q_0, r_0 or T_2/T_1, it is also implied that the shape of the flow field in Figure 4 is not affected by these parameters. Due to symmetry with respect to *AC* and also between FRPFM sorbent above and below the fracture plane, the following derivation (more specifically the choice of signs) is with respect to the flow field for segment *ABC* above the fracture. For the assumed direction of q_0, it is seen that flow enters across *BC* and leaves the sorbent across *AB*. AE_∞ and CF_∞ are stream lines acting like lateral no flow boundaries on Γ_2.

For purely advective transport in combination with linear and instantaneous sorption, the stream tube based method of *Klammler et al.* [2009] may be applied for particle travel time calculations. In the ζ_2-plane the travel time t between two points A and B on the same stream tube is known as $t = \int_A^B \frac{|d\zeta_2|}{|v|}$, where $|\cdot|$ denotes the absolute value of a vector or complex number, v [L/T] is the particle pore velocity at a location along the stream tube and $d\zeta_2$ is an infinitesimal element of a generally curved stream tube (Figure 4). By the property of continuity of flow between infinitesimal elements of different conformal mapping planes, it is further known that $2HnR|v||d\zeta_2| = |q_1||d\zeta_3|$, such that $t = \frac{2HnR}{q_1} \int_A^B \left|\frac{d\zeta_2}{d\zeta_3}\right|^2 |d\zeta_3|$. Here, H [L], n [−], and R [−] denote effective values of FRPFM layer (mesh plus sorbent plus external dye fabric) thickness, porosity, and tracer/contaminant retardation. The factor 2 in the numerator accounts for the division of $q_1 = |q_1|$ into two equal parts above and below the fracture intersection. This integral is now along straight stream lines in the ζ_3-plane (Figure A2) allowing for the simplification $|d\zeta_3| = dx$, where $x = r\cos\theta$. With $y = r\sin\theta$ and $|d\zeta_2/d\zeta_3|^2 = r_0^2/(x^2+y^2)$ from equation (A1), this leads to a travel time $t = \frac{2HnR}{q_1} \int_{x_0}^{x_\tau} \frac{r_0^2}{x^2+y^2} dx$ between points of abscissa x_0 and x_τ in the ζ_3-plane.

For further treatment, we define a dimensionless particle travel time as

$$\tau = \frac{tq_1}{2HnRr_0} \tag{A4}$$

which becomes equation (1) of the main text after substituting $q_1 = \alpha q_0$. By solving the travel time integral, τ may be expressed as

$$\tau = \frac{r_0}{y}\left(\arccos\frac{y}{r_0} + \arctan\frac{x_\tau}{y}\right) = \frac{r_0(\theta_0 - \theta_\tau)}{y} \tag{A5}$$

where $x_0 = -(r_0^2 - y^2)^{1/2}$ and θ_0 are the abscissa and angular coordinate of a tracer/contaminant particle at time $\tau = 0$ on the up-gradient limit *BC* of Γ_3, while x_τ and θ_τ are the abscissa and angular coordinate of the same particle at time $\tau > 0$. Equation (A5) may be inverted to express $x_\tau(\tau,y)$, i.e., particle location in Γ_3 for a given stream line and travel time.

$$x_\tau = y \tan\left(\tau\frac{y}{r_0} - \arccos\frac{y}{r_0}\right) \tag{A6}$$

By using $\zeta_3 = x_\tau + iy$ in equation (A1), resulting travel times or particle locations are mapped onto Γ_2, which results in the green isochrones in Figure 4 given as examples for different values of τ. Isochrones are lines of equal travel time and, under the assumptions made above, may be interpreted as particle fronts, which are pushed forward by water flow. In the case of initially present tracers/dye, the zone behind the front is cleared of all tracer/dye particles, while in the case of contaminants the opposite occurs (however, generally at different velocities due to different values of *R*). By letting *y* approach zero in equation (A6) and taking the limit, the respective coordinate of the tracer front in Γ_3 is found as $x_\tau = -r_0/(1+\tau)$. With this, equation (A3) and $r = |x_\tau|$ gives a maximum vertical dye mark width Δz_{dye} occurring near point *C* of

$$\Delta z_{dye} = 2r_0 \ln(1+\tau) \tag{A7}$$

where the factor 2 accounts for dye displacement above and below the fracture. Inversion of equation (A7) yields equation (4) as depicted by the thin continuous line in Figure 5.

The area A_{dye} [L^2] of the dye mark in Γ_2 may be found by integration in Γ_3 knowing that the local areal scaling factor between Γ_3 and Γ_2 is again $|d\zeta_2/d\zeta_3|^2 = r_0^2/(x^2+y^2)$. Introducing $m_{out} = A_{dye}/r_0^2$ [−] as a relative measure of dye loss gives

$$m_{out} = 4\left(\int_0^{y_{lim}}\int_{-\sqrt{r_0^2-y^2}}^{x_\tau}\frac{dxdy}{x^2+y^2} + \int_{y_{lim}}^{r_0}\int_{-\sqrt{r_0^2-y^2}}^{\sqrt{r_0^2-y^2}}\frac{dxdy}{x^2+y^2}\right) \tag{A8}$$

where the factor 4 accounts for symmetry between *ABC* and *CDA* in Figure A2 as well as for symmetry about the fracture plane (above and below). The first double integral in equation (A8) integrates along empty portions of all stream tubes, which still contain some tracer, and reduces to $\tau y_{lim}/r_0$ with x_τ from equation (A6). The second double integral corresponds to completely empty stream tubes and becomes zero for $y_{lim} = r_0$ (i.e., at $\tau = 0$). Thus, for small τ, equation (A8) becomes $m_{out} \approx 4\tau$, which is used in equation (3). For a general solution of m_{out} as a function of τ, equation (A8) is integrated numerically by dividing Γ_3 into a large number of grid points and summing $1/(x^2+y^2)$ for all grid points behind the dye/tracer front. The correspondence between y_{lim} and τ is given by equation (A5) with $y = y_{lim}$ and $(\theta_0 - \theta_\tau) = 2\arccos(y_{lim}/r_0)$. The result is depicted as the bold continuous line in Figure 5.

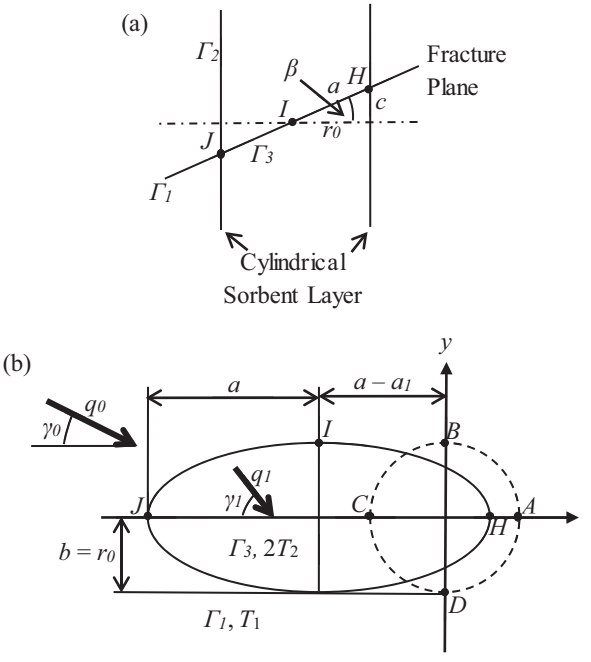

Figure B1. Nonperpendicular intersection between borehole and fracture plane. (a) Side view, and (b) view perpendicular to fracture plane.

Appendix B: Single Nonperpendicular Intersection

In general, the intersection between a fracture plane and a FRPFM axis is not perpendicular. For the common case

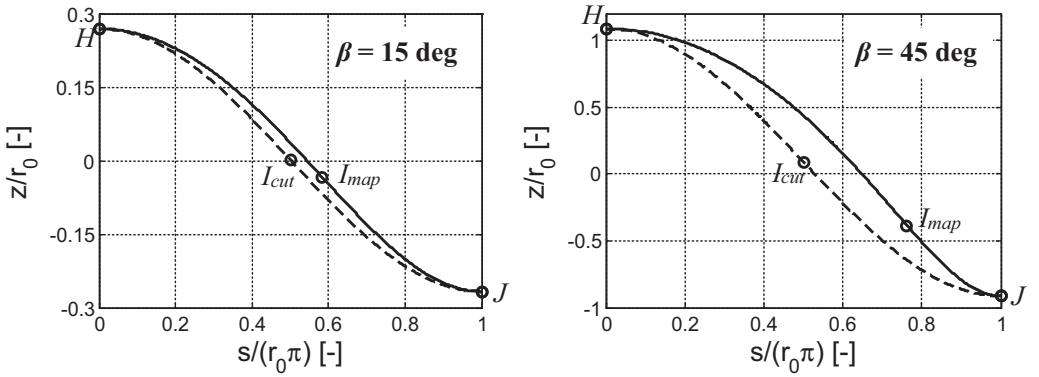

Figure B2. Differences between the unrolled sorbent-fracture intersection lines in Γ_2 from cutting the sorbent (physical cosine shape; dashed) and conformal mapping by equation (A1) (continuous) for $\beta = 15°$ and 45°.

of vertical boreholes, this means that the fracture dip angle β [−] with respect to the horizontal plane is larger than zero (Figure B1a). In such cases, the fracture intersects the sorbent along an ellipse of semi-major axis $a = r_0/\cos\beta$ [L] and semi-minor axis $b = r_0$ [L] (Figure B1b). After unrolling the sorbent layer, the intersection becomes a single period of a (co)sine of amplitude $c = r_0\tan\beta$. The loss of rotational symmetry prevailing at $\beta = 0$ further introduces the undisturbed fracture flow direction γ_0 [L] as an additional variable (defined here with respect to the orientation of the long axis; Figure B1b). Given these complexities we investigate the usefulness of equation (A1) to generalize the results from Appendix A in an approximate way. For this purpose, similar to Figure A2, the elliptical (and fictitious) flow domain Γ_3 within the fracture is located as shown in Figure B1b, where the offset parameter a_1 in *x*-direction is obtained from equation (A3) and imposing that the difference in *z*-coordinates between the images of points *H* and *J* in Γ_2 be equal to 2*c*.

$$a_1 = \frac{2r_0}{\cos\beta[1+\exp(2\,\tan\beta)]} \tag{B1}$$

The image of the (half) ellipse *HIJ* after mapping onto Γ_2 is graphically illustrated by the continuous lines in Figure B2 for two exemplary inclination angles of $\beta = 15$ and 45 degrees (note that the shifting along *z* has no impact for our problem). For comparison, Figure B2 also contains dashed lines corresponding to the true (physical) cosine shape of the sorbent-fracture intersection after rolling the FRPFM sorbent out flat. Besides the overall shape, also the locations of points along the curves have to (approximately) coincide, as illustrated by the example of point *I*. While for $\beta = 0$ the result becomes identical to the exact mapping of Figure A1 and A2, the approximation for $\beta > 0$ is considered reasonable, in particular for the range $\beta \leq 45°$ shown. Consequently, the same (but now approximate) argument may be applied as with circular intersections, namely that the flow field in Γ_2, obtained from conformal mapping of a known flow

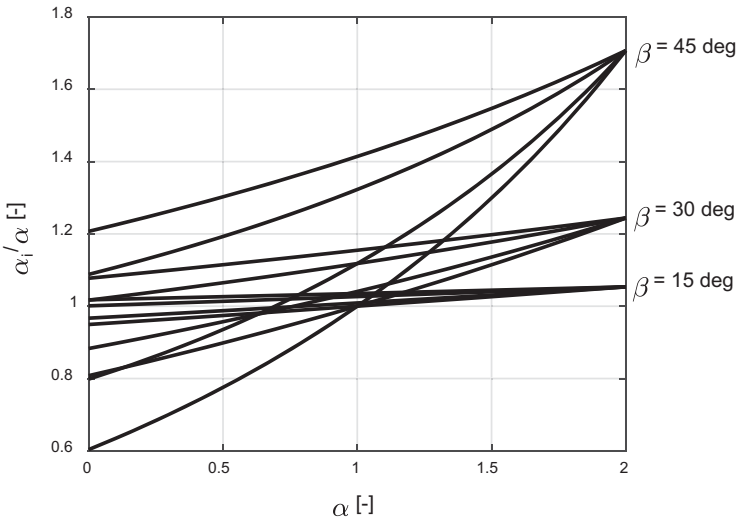

Figure B3. Influence of fracture plane inclination on flow convergence through sorbent layer expressed by α_i/α as a function of α for different values of β and $\gamma_0 = \{0, 30, 60, 90\}$ degrees for graphs from bottom up.

field in Γ_3, may be "cut out" of the piece of paper it is plotted on, rolled up and located at an angle β along *HIJ* in Figure instead of Γ_3 without disturbing the flow field in Γ_1.

The flow field inside the ellipse Γ_3 is known to be uniform of angle γ_1 [L] and total flow Q [L^3/T] given by [*Strack*, 1989; *Kacimov et al.*, 2011]

$$\gamma_1 = \arctan\left(\frac{1+\lambda\varepsilon}{1-\lambda\varepsilon}\tan\gamma_0\right) \tag{B2}$$

$$Q = 2q_0 a\cos\gamma_0 \frac{1-\lambda}{1-\lambda\varepsilon}\sqrt{\left[\frac{b(1-\lambda\varepsilon)}{a(1+\lambda\varepsilon)}\right]^2 + \tan^2\gamma_0} \tag{B3}$$

where $\varepsilon = (a-b)/(a+b) = (1-\cos\beta)/(1+\cos\beta)$ and $\lambda = (T_1 - 2T_2)/(T_1 + 2T_2) = 1-\alpha$. For simplicity, and given the approximations involved above, we limit attention to the short time approximation of linear tracer loss, which is valid as long as the portion of Q not eluting any tracer is negligible. Under this premise $m_{out} = Qt/(HnR_{tra}r_0^2)$, such that an expression for q_0 may be found after substituting equation (B3). Comparison of the result to equation (1) shows that a flow convergence factor α_i [−] for inclined fractures may be found as

$$\alpha_i = \frac{\cos\gamma_0}{\cos\beta}\frac{\alpha}{1-(1-\alpha)\varepsilon}\sqrt{\left[\cos\beta\frac{1-(1-\alpha)\varepsilon}{1+(1-\alpha)\varepsilon}\right]^2 + \tan^2\gamma_0} \tag{B5}$$

such that equations (1) and (7) remain applicable if α_i is used instead of α. Equation (B5) is a function of α, β, and γ_0; it is graphically represented in Figure B3 for some exemplary cases. Hereby, β and γ_1 may be obtained from inspection of the visual dye mark, and γ_0 is computed from equation (B2). For perpendicular intersections $\beta = \varepsilon = 0$, such that equation (B5) correctly reduces to $\alpha_i = \alpha$. The parameter a_1 from equation (B1) is only required to evaluate the approximation taken in Figure B2, but not for FRPFM interpretation.

Appendix C: Nearby Packers or Multiple Equidistant Perpendicular Intersections

In practice, more than a single fracture may intersect a FRPFM, or the finite distance between top and bottom packers may become relevant. Both conditions affect the flow fields inside the sorbent and the fractures. Here we consider the simplest case of a large number of perpendicular intersections of constant separation distance and of equal transmissivities T_1 exposed to a uniform gradient. Thus, the center plane between two fractures becomes a no-flow boundary in the sorbent flow domain Γ_2 of Figure A1 and the situation is identical to the one of a horizontal fracture plane centered between two nearby impermeable packers. Denoting the distance between neighboring fractures (or packers) by d [L] this no-flow boundary corresponds to a horizontal line at $z = d/2$ in Figure A1. By equation (A3) this translates into a circular no-flow boundary at $r = r_0/\exp[d/(2r_0)]$ in Γ_3 of Figure A2. Using *Klammler et al.* [2007] this additional no-flow

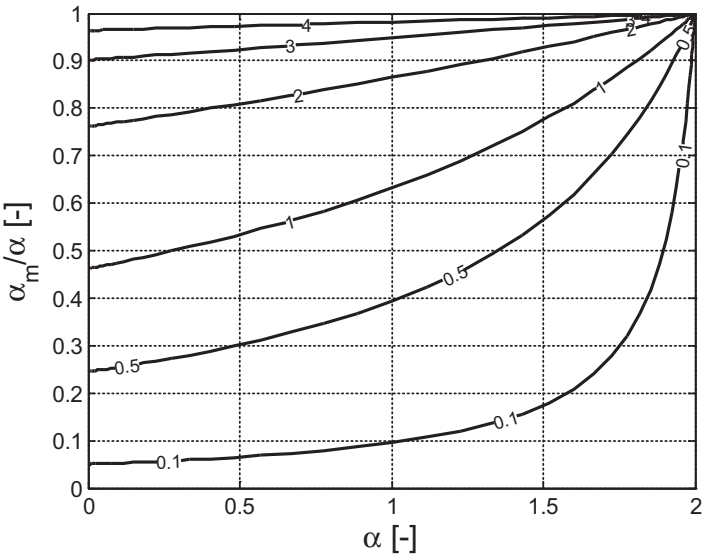

Figure C1. Influence of distance between horizontal fracture planes or to nearby impermeable packers on flow convergence through sorbent layer expressed by α_m/α as a function of α for different values of d/r_0 indicated on the contour lines.

boundary may be accounted for by converting Γ_3 into an equivalent homogeneous circular flow domain (i.e., eliminating the no-flow boundary) of effective transmissivity T_{2m} given by

$$T_{2m} = T_2 \frac{\exp\left(\frac{d}{r_0}\right) - 1}{\exp\left(\frac{d}{r_0}\right) + 1} \tag{C1}$$

which collapses to $T_{2m} = T_2$ for the single intersection (or distant packer) case where $d/r_0 \gg 1$. Thus, T_{2m} from equation (C1) may be used instead of T_2 in equation (2) to obtain a flow convergence factor α_m [−] for multiple perpendicular fracture intersections or nearby packers of separation d as

$$\alpha_m = \frac{2}{1 + \frac{T_1}{2T_{2m}}} \tag{C2}$$

Other than the use of α_m instead of α in equations (1) and (7), the short time (linear) approximations for estimating q_0 and J are not affected by d/r_0. The impact of d/r_0 on flow convergence in terms of the ratio α_m/α is illustrated by Figure C1.

Acknowledgments
This research was funded by the U.S. Department of Defense (project number ER0831) under the Environmental Security Technology Compliance Program (ESTCP) and the U.S. National Science Program (Award number 0804134). This paper has not been subject to DoD review and accordingly does not necessarily reflect the views of the DoD. Data from experiments presented may be obtained by contacting the first or second author.

References

Acar, Ö., et al. (2013), A stochastic model for estimating groundwater and contaminant discharges from fractured rock passive flux meter measurements, *Water Resour. Res.*, *49*, 1–15.
Annable, M. D., K. Hatfield, J. Cho, H. Klammler, B. Parker, J. Cherry, and P. S. C. Rao (2005), Field-scale evaluation of the passive flux meter for simultaneous measurement of groundwater and contaminant fluxes, *Environ. Sci. Technol.*, *39*(18), 7194–7201.
Berkowitz, B. (2002), Characterizing flow and transport in fractured geological media: a review, *Adv. Water Resour.*, *25*(8-12), 861–884.
Cherry, J. A., B. L. Parker, and C. Keller (2007), A new depth-discrete multilevel monitoring approach for fractured rock, *Ground Water Monit. Remed.*, *27*(2), 57–70.
Coleman, I. T., B. L. Parker, C. H. Maldaner, and M. H. Mondanos (2015), Groundwater flow characterization in a fractured bedrock aquifer using active DTS tests in sealed boreholes, *J. Hydrol.*, *528*, 449–462.
Department of Energy (1993), Technology information profile (rev. 2) for ProTech, technology name—Colloidal borescope. DOE ProTech Database, Oak Ridge National Laboratory, TTP Reference Number OR-11211-04, July 15, 1993.
Garcia Gutierrez, M., J. Guimera, A. Yllera de Llano, A. Hernandez Benitez, J. Humm, and M. Saltink (1997), Tracer test at El Berrocal site, *J. Contamin. Hydrol.*, *26*(1-4), 179–188.
Hatfield, K., M. Annable, J. Cho, P. S. C. Rao, and H. Klammler (2004), A direct passive method for measuring water and contaminant fluxes in porous media, *J. Contamin. Hydrol.*, *75*(3-4), 155–181.
ITRC (Interstate Technology & Regulatory Council) (2010), Use and Measurement of Mass Flux and Mass Discharge, MASSFLUX-1, Washington, D. C.: Interstate Technology & Regulatory Council, Integrated DNAPL Site Strategy Team. [Available at www.itrcweb.org.]
Kerfoot, W. B. (1992), The use of flowmeters and slow release dyes to determine bedrock flow for wellhead protection, in *Proceedings, The Sixth National Outdoor Action Conference on Aquifer Restoration, Ground Water Monitoring and Geophysical Methods, National Groundwater Association*, pp. 755–763, May 11–13, 1992, Las Vegas, Nev.
Klammler, H., K. Hatfield, M. D. Annable, E. Agyei, B. Parker, J. Cherry, and P. S. C. Rao (2007), General analytical treatment of the flow field relevant to the interpretation of passive fluxmeter measurements, *Water Resour. Res.*, *43*, W04407.
Klammler, H., K. Hatfield, and I. Perminova (2009), Groundwater and contaminant travel time distributions near permeable reactive barriers, in *Water Resources Management*, edited by V. C. A. Brebbia, V. Popov, WIT Transactions on Ecology and the Environment, vol. 125, 245–256.
Neuman, S. P. (2005), Trends, prospects and challenges in quantifying flow and transport through fractured rocks, *Hydrogeol. J.*, *13*, 124–147.
Novakowski, K., G. Bickerton, P. Lapcevic, J. Voralek, and N. Ross (2006), Measurements of groundwater velocity in discrete rock fractures, *J. Contamin. Hydrol.*, *82*(1-2), 44–60.
Parker, B. L., J. A. Cherry, and S. W. Chapman (2012), Discrete fracture network approach for studying contamination in fractured rock, *AQUAMundi: J. Water Sci.*, *60*(52), 101–116.
Pedler, W. H., C. L. Head, and L. L. Williams (1992), Hydrophysical logging - A new wellbore technology for hydrogeologic and contaminant characterization of aquifers, in *Proceedings, The Sixth National Outdoor Action Conference on Aquifer Restoration, Ground Water Monitoring, and Geophysical Methods, National Ground Water Association*, pp. 701–715, May 11–13, 1992, Las Vegas, Nev.
Pehme, P. E., B. L. Parker, J. A. Cherry, and J. P. Greenhouse (2010), Improved resolution of ambient flow through fractured rock with temperature logs, *Ground Water, 28*(2), 191–211.
Pehme, P. E., B. L. Parker, J. A. Cherry, J. Molson, and J. P. Greenhouse (2013), Enhanced detection of hydraulically active fractures by temperature profiling in lined heated bedrock boreholes, *J. Hydrol.*, *484*, 1–15.
Pehme, P. E., B. L. Parker, J. A. Cherry, and D. Blohm (2014), Detailed measurement of the magnitude and orientation of thermal gradients in lined boreholes for characterizing groundwater flow in fractured rock, *J. Hydrol.*, *513*, 101–114.
Shapiro, A. M. (2002), Cautions and suggestions for geochemical sampling in fractured rock, *Groundwater Monit. Remed.*, *22*(3), 151–164.
Shapiro, A. M., P. A. Hsieh, W. C. Burton, and G. J. Walsh (2007), Integrated multi-scale characterization of groundwater flow and chemical transport in fractured crystalline rock at the Mirror Lake Site, New Hampshire, in *Subsurface Hydrology: Data Integration for Properties and Processes*, edited by D. W. Hyndman, F. D. Day-Lewis, and K. Singha, pp. 201–225, AGU, Washington, D. C.
SonTek (1996), Modified ADV for 3D velocity measurements in boreholes—Final project report, U.S. Geological Survey Contract Number 1434-95-C-40232, 29 pp.
Sterling, S. N., B. L. Parker, J. A. Cherry, J. H. Williams, J. W. Lane Jr., and F. P. Haeni (2005), Vertical cross contamination of trichloroethylene in a borehole in fractured sandstone, *Ground Water*, *43*(4), 557–573.

Strack, O. D. L. (1989), *Groundwater Mechanics*, Prentice Hall, N. Y.

Stucker, V., J. Ranville, M. Newman, A. Peacock, J. Cho, and K. Hatfield (2011), Evaluation and application of anion exchange resins to measure groundwater uranium flux at a former uranium mill site, *Water Res.*, *45*(16), 4866–4876.

Tsang, C. F., P. Hufschmied, and F. V. Hale (1990), Determination of fracture inflow parameters with a borehole fluid conductivity logging method, *Water Resour. Res.*, *26*(4), 561–578.

Wilson, J. T., W. A. Mandell, F. L. Paillet, E. R. Bayless, R. T. Hanson, P. M. Kearl, W. B. Kerfoot, M. W. Newhouse, and W. H. Pedler (2001), An Evaluation of Borehole Flowmeters Used to Measure Horizontal Ground-Water Flow in Limestones of Indiana, Kentucky, and Tennessee: U.S. Geological Survey Water-Resources Investigations Report 01-4139, 129 pp.

Xu, Y., G. J. van Tonder, B. van Wyk, E. van Wyk, and B. Aleobua (1997), Borehole dilution experiment in a Karoo aquifer in Bloemfontein, *Water SA*, *23*(2), 141–145.